

Supporting Information

Asymmetric Cross-Orbital Coupling in Fe-Mn Spinels Decouples Structural Stability and Kinetics in Sodium-Ion Storage

*Shuyun Yao^{a,b}, Jingyu Wu^a, Feike Zhang^a, Zhiyu Yang^a, Xiaojiang Yu^c, Shibo Xi^d, Qian He^e, Yao Wu^e, Zhiqun Lin^{*b}, & Yi-Ming Yan^{*a}*

^a State Key Lab of Organic-Inorganic Composites, Beijing Advanced Innovation Center for Soft Matter Science and Engineering, Beijing University of Chemical Technology, Beijing, 100029, People's Republic of China

^b Department of Chemical and Biomolecular Engineering, National University of Singapore, 4 Engineering Drive 4, Singapore, 117585 Singapore

^c Synchrotron Light Source, National University of Singapore, 5 Research link, 117603, Singapore

^d Institute of Chemical and Engineering Sciences, A*STAR (Agency for Science, Technology and Research), 1 Pesek Road, Jurong Island, 627833, Singapore

^e Department of Materials Science and Engineering, National University of Singapore, Singapore, 117574, Singapore

*Corresponding Authors:

E-mail: yanym22@mail.buct.edu.cn; z.lin@nus.edu.sg

Table of Contents

1. Experimental Procedures.....	5
2. Chemicals and Materials.....	5
3. Preparation of Electrode.....	5
4. Characterizations.....	5
5. Electrochemical Measurements.....	6
6. Mechanical Flexibility of Electrodes.....	6
7. EIS analysis at different temperatures.....	7
8. Kinetic calculation.....	7
9. The charge storage mechanism of $K_xFe_yMn_{1-y}O_z$	7
10. Supercapacitor device measurements.	8
11. DFT Methods.	8
12. Figure S1. Schematic illustration of the variations in TM-O bond lengths and K-O distances in $K_xFe_yMn_{1-y}O_z$ spinel materials ($Y = 0, 0.09, 0.15, 0.22$)..	10
13. Figure S2. GCD curves of a series of $K_xFe_yMn_{1-y}O_z$ spinel materials ($Y = 0, 0.09, 0.15, 0.22$) at $1 A g^{-1}$	11
14. Figure S3. Cycling stability of a series of $K_xFe_yMn_{1-y}O_z$ spinel materials ($Y = 0, 0.09, 0.15, 0.22$) at a current density of $1 A g^{-1}$	12
15. Figure S4. Schematic illustration of the asymmetric cross-orbital coupling between Fe_{Oh} and Mn_{Oh} in $K_xFe_yMn_{1-y}O_z$ spinel materials.	13
16. Figure S5. Hybridization degrees of a series of $K_xFe_yMn_{1-y}O_z$ spinel materials ($Y = 0, 0.09, 0.15, 0.22$)..	14
17. Figure S6. PDOS plots of the Mn 3d and Fe 3d orbitals of (a) KMO, (b) $KF_{0.15}M_{0.85}O$ and (c) $KF_{0.22}M_{0.78}O$	15
18. Figure S7. PDOS plots of the Mn 3d and O 2p orbitals of (a) KMO, (b) $KF_{0.15}M_{0.85}O$ and (c) $KF_{0.22}M_{0.78}O$	16
19. Figure S8. SEM images of (a) KMO, (b) $KF_{0.15}M_{0.85}O$ and (c) $KF_{0.22}M_{0.78}O$	17
20. Figure S9. TEM images of (a) KMO and (b) $KF_{0.15}M_{0.85}O$ powder..	18
21. Figure S10. HR-TEM images of (a) KMO and (b) $KF_{0.15}M_{0.85}O$ powder.....	19
22. Figure S11. EDS mapping of $KF_{0.15}M_{0.85}O$ powder.....	20

23. Figure S12. XPS valence band spectra of KMO and $\text{KF}_{0.15}\text{M}_{0.85}\text{O}$	21
24. Figure S13. UPS of KMO and $\text{KF}_{0.15}\text{M}_{0.85}\text{O}$	22
25. Figure S14. (a) UV-vis diffuse reflectance spectra and (b) bandgap energy of KMO and $\text{KF}_{0.15}\text{M}_{0.85}\text{O}$	23
26. Figure S15. Measurement of the electrical conductivity of KMO and $\text{KF}_{0.15}\text{M}_{0.85}\text{O}$ using the four-probe method.....	24
27. Figure S16. CV curves of KMO and $\text{KF}_{0.15}\text{M}_{0.85}\text{O}$ at 5 mV s^{-1}	25
28. Figure S17. CV curves of (a) KMO and (b) $\text{KF}_{0.15}\text{M}_{0.85}\text{O}$ electrode at different scan rates from 5 to 50 mV s^{-1}	26
29. Figure S18. GCD curves of (a) KMO and (b) $\text{KF}_{0.15}\text{M}_{0.85}\text{O}$ electrode at 1 A g^{-1}	27
30. Figure S19. Nyquist plots of KMO and $\text{KF}_{0.15}\text{M}_{0.85}\text{O}$ in the pristine state.....	28
31. Figure S20. EIS study of KMO at varied temperatures.....	29
32. Figure S21. Capacity contribution from diffusion-controlled and surface-controlled processes at different scan rates for (a) KMO and (b) $\text{KF}_{0.15}\text{M}_{0.85}\text{O}$	30
33. Figure S22. Energy curves and structures for Na^+ diffusion in KFMO and KMO models. The barriers in the energy curves are highlighted by a blue font. The purple, green, red, lavender and yellow colors represent the K, Fe, O, Mn and Na atoms, respectively.....	31
34. Figure S23. In situ Raman spectra of (a) KMO and (b) KFMO electrode during the first charge/discharge cycle.	32
35. Figure S24. In-situ XRD patterns showing the peak shifts of the (003), and (005) planes for (a-b) KFMO and (c-d) KMO.	33
36. Figure S25. The cross-sectional SEM image of (a) $\text{KF}_{0.15}\text{M}_{0.85}\text{O}$ and (b) KMO after 200 cycles. The cross-sectional sample was prepared via the technology of focused ion beam (FIB).....	34
37. Figure S26. Local magnified SEM cross-sectional image of (a) $\text{KF}_{0.15}\text{M}_{0.85}\text{O}$ and (b) KMO after 200 cycles. The cross-sectional sample was prepared via the technology of focused ion beam (FIB).....	35
38. Figure S27. EDS elemental mapping of the KFMO electrode after 200 electrochemical cycles....	36
39. Figure S28. Comparative analysis: $\text{KF}_{0.15}\text{M}_{0.85}\text{O}$ cathode versus previous studies.....	37
40. Figure S29. Schematic illustration of ASC based on $\text{KF}_{0.15}\text{M}_{0.85}\text{O}$ cathode and AC anode.....	38
41. Figure S30. CV profiles of $\text{KF}_{0.15}\text{M}_{0.85}\text{O}$ and AC in $1.0 \text{ M Na}_2\text{SO}_4$	39
42. Figure S31. (a) CV profiles at varied potential ranges at 100 mV s^{-1} . (b) CV curves of $\text{KF}_{0.15}\text{M}_{0.85}\text{O}$ //AC ASC at various scan rates.....	40

43. Figure S32. Comparative analysis of stability, power density, and energy density against previously reported results.....	41
44. Table S1. Element contents of the samples obtained from element analysis Wt.%.....	42
45. Table S2. The d-electrons states proportion in $K_xFe_yMn_{1-y}O_z$ obtained from DOS.....	43
46. Table S3. -COHP analysis of KMO, $KF_{0.15}M_{0.85}O$ and $KF_{0.22}M_{0.78}O$	44
47. Table S4. Fitting results of KMO and KFMO samples obtained from the EIS curves.....	45
48. Supplementary References.....	46

Experimental Procedures

Chemicals and Materials

Potassium carbonate (K_2CO_3 , 99%), Manganese (III) oxide (Mn_2O_3 , 99%), and Iron (III) oxide (Fe_2O_3 , 99%) were obtained from Sigma-Aldrich. Anhydrous (Na_2SO_4) were purchased from Beijing Tong Guang Fine Chemicals Company. All reagents were used as received without further purification. And all solutions were prepared using ultrapure water (resistance = 18.2 $M\Omega$ cm).

Preparation of Electrode

A series of Fe-doped $K_xMn_yO_z$ spinel materials (denoted as $K_xFe_yMn_{1-y}O_z$, where y represents the molar ratio of Fe to Mn; $y = 0, 0.09, 0.15, 0.22$) were synthesized via a conventional solid-state reaction. Stoichiometric amounts of K_2CO_3 , Mn_2O_3 , and Fe_2O_3 precursors were thoroughly ground in an agate mortar with excess K_2CO_3 to ensure homogeneous mixing. The resulting mixtures were subsequently calcined in a muffle furnace under ambient air at $900^\circ C$ for 24 h, with a controlled heating rate of $2^\circ C\ min^{-1}$. After natural cooling to room temperature, the final products were collected and stored in an argon-filled glove box to prevent moisture absorption and oxidative degradation.

Characterization

Microstructures were studied using scanning electron microscopy (SEM, FEI Quanta 200) at 20 kV, transmission electron microscopy (TEM; FEI Tecnai G220). Scanning transmission electron microscopy (STEM) images were acquired using a FEI Talos F200X and a JEOL JEM-ARM200F, both operated at 200 kV. The elemental analyses of the samples were performed by EDS mapping. The crystallographic phases of samples were determined by a Rigaku D/max 2500 X-ray powder diffractometer with Cu $K\alpha$ -radiation ($\lambda = 0.15405\ nm$). The electronic structure and compositional information on the samples were investigated by X-ray photoelectron spectroscopy (XPS, ESCALAB 250). Raman spectra of the sample (one spectrum

per 30 s) were captured while a cyclic voltammetry test was at a scan rate of 2 mV s^{-1} simultaneously. Soft X-ray absorption spectroscopy (sXAS) is performed at room temperature and at the $L_{2,3}$ edges of Mn, Fe, and O K edge in the energy ranges from 630 to 665 eV, 700 to 735 eV and 525 to 550 eV, respectively, at the SINS beamline of the Singapore Synchrotron Light Source. The incident angles (θ), relative to the surface normal, are chosen at $\theta = 50^\circ$. All spectra are collected in total-electron-yield (TEY) detection mode with a photon energy resolution of 0.5 eV, and the degree of the circular polarization is 88%. The probing depth is expected to be $<10 \text{ nm}$. For the in-situ XRD characterization, we used a beryllium-window-equipped in-situ cell holder to record real-time data of the half-cell. Each scan was conducted over a 10° - 80° range with a step size of 0.02° and a scanning speed of $0.04^\circ/\text{s}$. The in-situ cell was continuously charged and discharged without any interval between scans. Additionally, no smoothing procedures were applied to the data to preserve the integrity of the original measurements.

Electrochemical Measurements

The working electrode was prepared by the traditional slurry-coating method. 80 wt% active material, 10 wt% acetylene black, and 10 wt% polytetrafluoroethylene (PTFE) was mixed and coated onto carbon cloth with an area of 1 cm^2 . The electrode was then heated at 60°C for 2 hours to evaporate the solvent and used as the working electrode. Electrochemical measurements were conducted in a general three-electrode configuration in 1.0 M Na_2SO_4 aqueous electrolyte with Ag/AgCl and a Pt foil as reference electrode and counter electrode, respectively.

Mechanical Flexibility of Electrodes

Although this study mainly focuses on tuning the electronic structure of $\text{K}_x\text{Fe}_y\text{Mn}_{1-y}\text{O}_2$ to enhance electrochemical performance, we acknowledge that mechanical adaptability is also important for practical applications. In our work, the spinel powders were directly coated onto flexible carbon cloth, resulting in electrodes with overall good mechanical compliance.

While the active material itself was not specifically designed for flexibility, the electrode architecture benefits from the inherent flexibility of the substrate. We recognize that evaluating the intrinsic mechanical properties of the spinel phase (e.g., bending durability or stress-strain behavior) is valuable for future studies aimed at flexible or wearable energy storage devices.

EIS analysis at different temperatures

According to the relationship, the charge transfer resistance (R_{ct}) follows based on a thermally activated process. The Arrhenius equation is applied for calculation **Equation (S1)**.

$$1/R_{ct} = A_0 \exp(-E_a/RT)$$

where A_0 , E_a , T , and R represent a constant, the activation energy, temperature in Kelvin, and gas constant, respectively.

Kinetic calculation

Capacitance contribution can be qualitatively analysed according to the CV curve, as shown below in **Equation (S2)**¹:

$$i = av^b$$

where i and v are the current density and the potential scan rate, respectively, a is a constant and b is a tuneable parameter with a value of 0.5-1.0. When the value of b is close to 1.0, the reaction process is dominated by surface capacitance; when the value of b is close to 0.5, the reaction process is dominated by diffusion control.

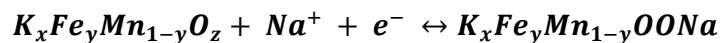
The contribution of capacitance and diffusion limit to the total capacitance is further quantified.

$$i(V) = k_1v + k_2v^{1/2}$$

where k_1 and k_2 represent capacitive and diffusion contributions, respectively.

The charge storage mechanism of $K_xFe_yMn_{1-y}O_z$

$K_xFe_yMn_{1-y}O_z$ can store charge by fast and reversible redox reaction on the electrode/electrolyte interface in neutral Na_2SO_4 electrolyte during charge and discharge process according to **Equation (S3)**²:



During the cycling process, the redox activity of $K_xFe_yMn_{1-y}O_z$ is primarily attributed to the Mn element. In the discharging process, Mn is reduced from a higher oxidation state to a lower one, accompanied by the generation of $K_xFe_yMn_{1-y}OONa$. In the charging process, Mn is oxidized from a lower oxidation state to a higher one, along with the transformation of $K_xFe_yMn_{1-y}OONa$ into $K_xFe_yMn_{1-y}O_z$.

Supercapacitor device measurements

An asymmetric supercapacitor (ASC) device was fabricated by employing $K_xFe_yMn_{1-y}O_z$ and AC as anode and cathode, respectively. Two electrodes were separated by a glassy fibrous separator in 1 M Na_2SO_4 aqueous electrolyte. Cyclic voltammetry (CV) and galvanostatic charge/discharge (GCD) measurements were performed in a potential window of 0 to 2.4 V.

The corresponding calculation formula **(S4)** is as follows^{3, 4}:

$$C = \frac{\text{Area}}{(V_2 - V_1) \times m \times v}$$

The energy density (E, Wh kg^{-1}) of the ASC is calculated according to **Equation (S5)**:

$$E = \frac{C \times (V_2 - V_1)^2}{2} \times \frac{1000}{3600}$$

where Area, V_1 - V_2 , m and v are the mathematical integration area under the CV curve, voltage window (V), mass (g) and scan rate (V/s), respectively.

DFT Methods

All spin polarization calculations were performed using the Vienna Ab Initio simulation package (VASP)⁵. The electron-ion interaction was described with the projector augmented wave (PAW) method. The electron exchange and correlation energies were treated within the generalized gradient approximation in the Perdew-Burke-Ernzerh of formalism (GGA-PBE)⁶.

In order to more accurately describe the d orbitals of transition metals, the GGA+U method was used. The effective U values given to Fe and Mn ions were 5.3 eV, and 4.0 eV, respectively. The computational process also encompassed magnetic calculations, with Mn and Fe values set at 2 each. In structural optimization, the plane wave cutoff energy is considered to be 500 eV. The convergence accuracy of the iterative process (SCF) is 10^{-5} . The strongest convergence exponent acting on an atom is 0.001 eV atom. When selecting K points for calculation, we choose a 6×6×6 inverted space grid for calculation and the thickness of the vacuum layer is set to about 15 angstroms. While the KMO crystal consists of 27 Mn, 52 O, and 8 K atoms; the $\text{KF}_{0.09}\text{Mn}_{0.91}\text{O}$ is composed of 25 Mn, 2 Fe, 52 O, and 8 K atoms; $\text{KF}_{0.15}\text{Mn}_{0.85}\text{O}$ is composed of 23 Mn, 4 Fe, 52 O, and 8 K atoms; $\text{KF}_{0.22}\text{Mn}_{0.78}\text{O}$ is composed of 21 Mn, 6 Fe, 52 O, and 8 K atoms; Every atom in these models underwent relaxation. To determine the energy barrier for Na^+ migration, a CINEB calculation was executed. To study Na^+ diffusion and to preclude electrostatic repulsion among distinct Na ions, two models were devised, each containing a singular Na atom. During the CINEB procedure, all atoms were permitted to relax within the set lattice parameters.

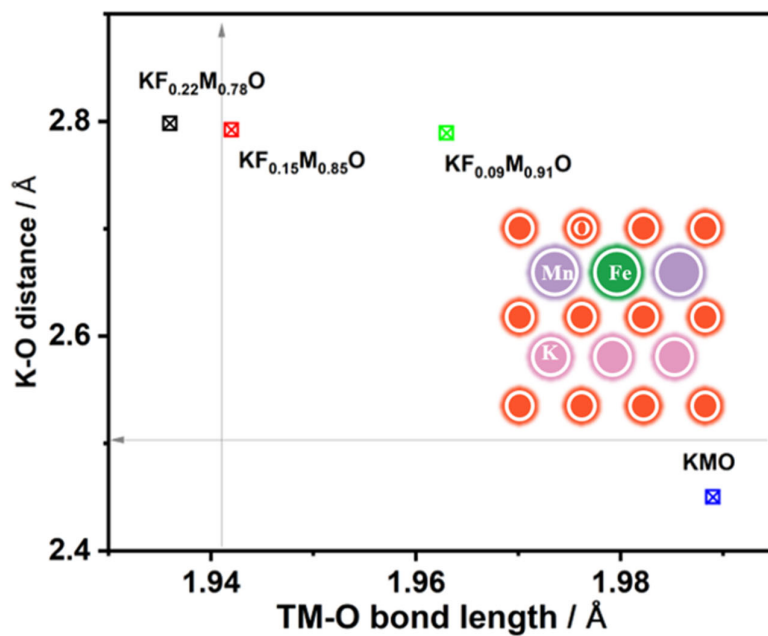


Figure S1. Schematic illustration of the variations in TM-O bond lengths and K-O distances in $\text{K}_x\text{Fe}_y\text{Mn}_{1-y}\text{O}_z$ spinel materials ($Y = 0, 0.09, 0.15, 0.22$).

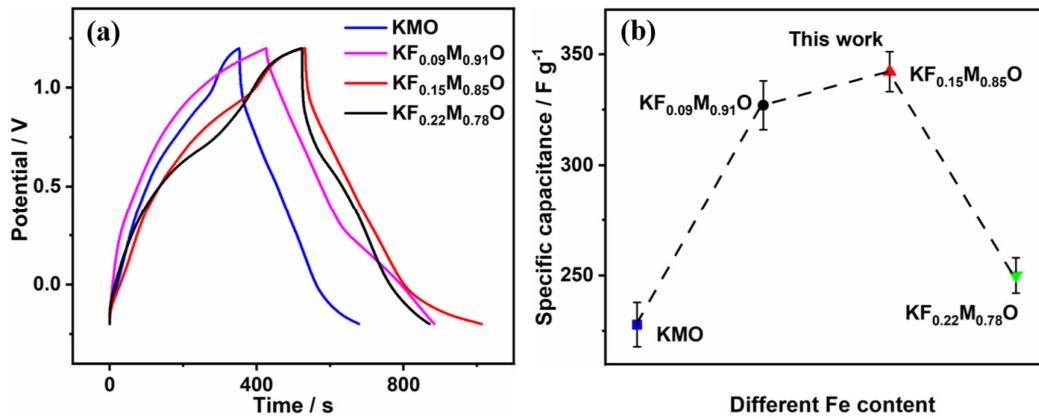


Figure S2. GCD curves of a series of $\text{K}_x\text{Fe}_y\text{Mn}_{1-y}\text{O}_z$ spinel materials ($Y = 0, 0.09, 0.15, 0.22$) at 1 A g^{-1} .

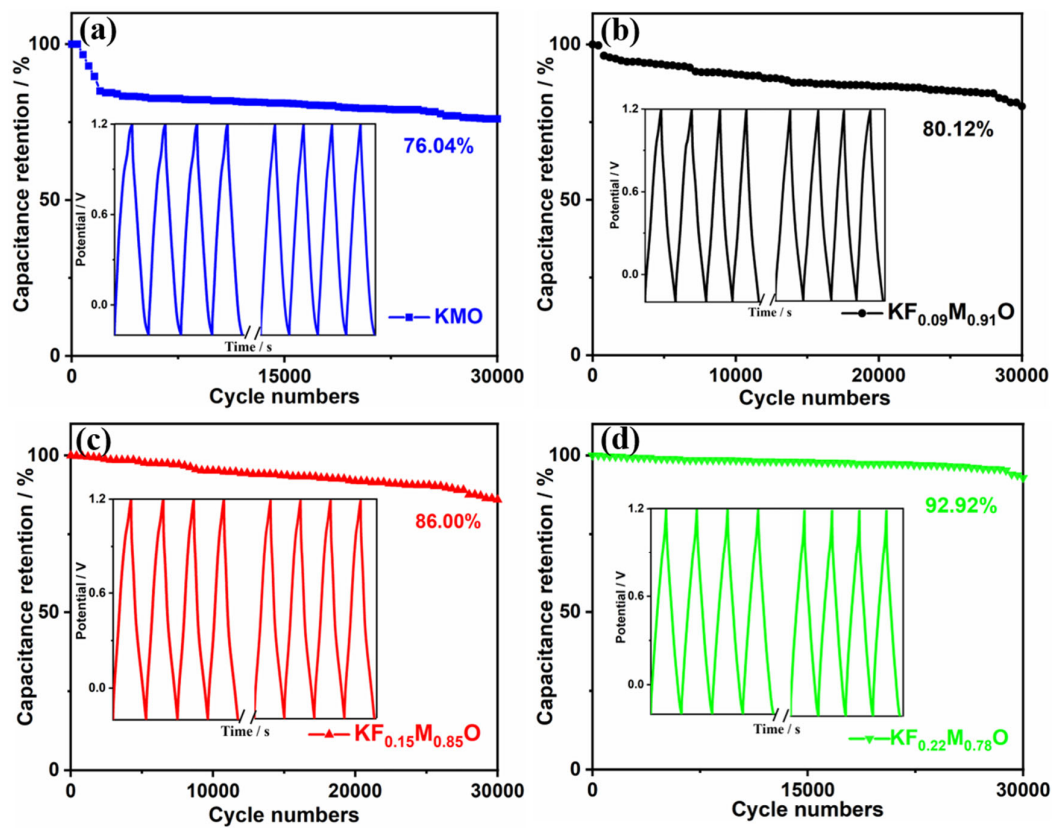


Figure S3. Cycling stability of a series of $K_xFe_yMn_{1-y}O_z$ spinel materials (Y = 0, 0.09, 0.15, 0.22) at a current density of 1 A g^{-1} .

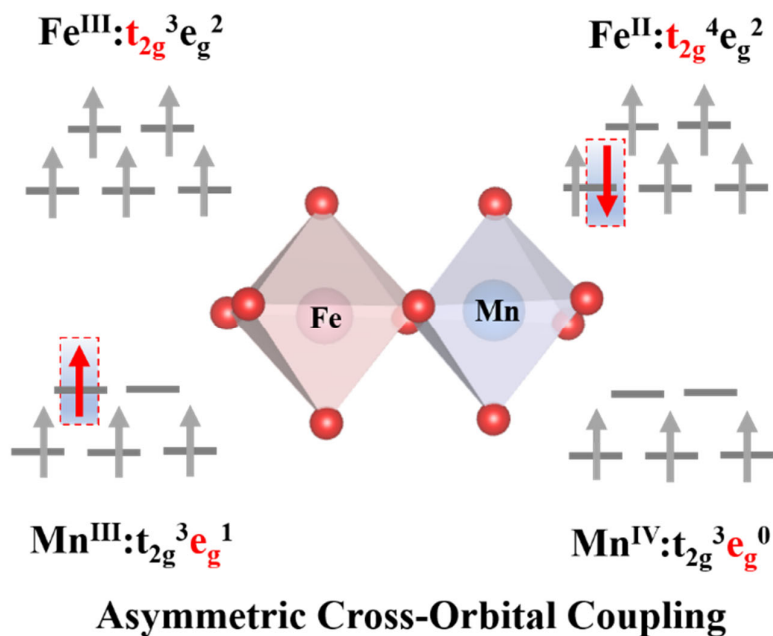


Figure S4. Schematic illustration of the asymmetric cross-orbital coupling between Fe_{Oh} and Mn_{Oh} in $\text{K}_x\text{Fe}_y\text{Mn}_{1-y}\text{O}_z$ spinel materials.

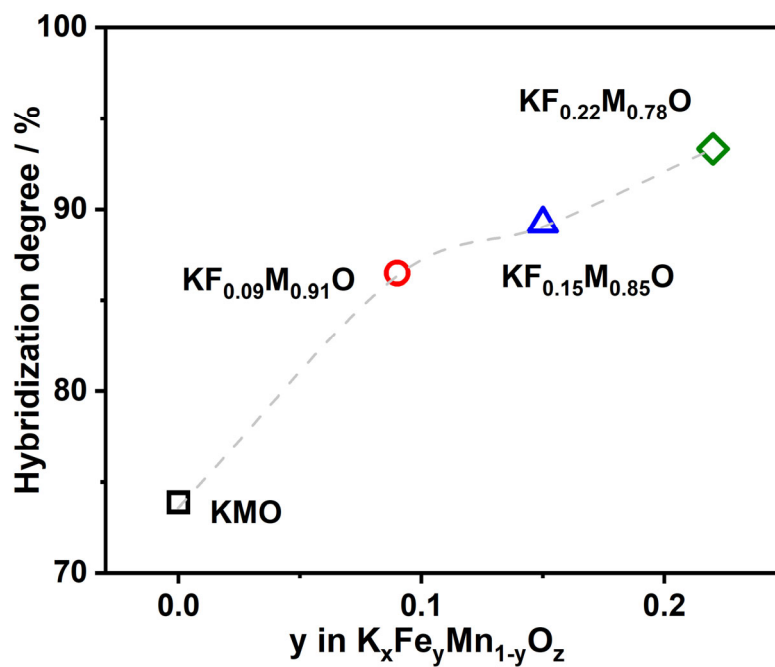


Figure S5. Hybridization degrees of a series of $K_x Fe_y Mn_{1-y} O_z$ spinel materials ($Y = 0, 0.09, 0.15, 0.22$).

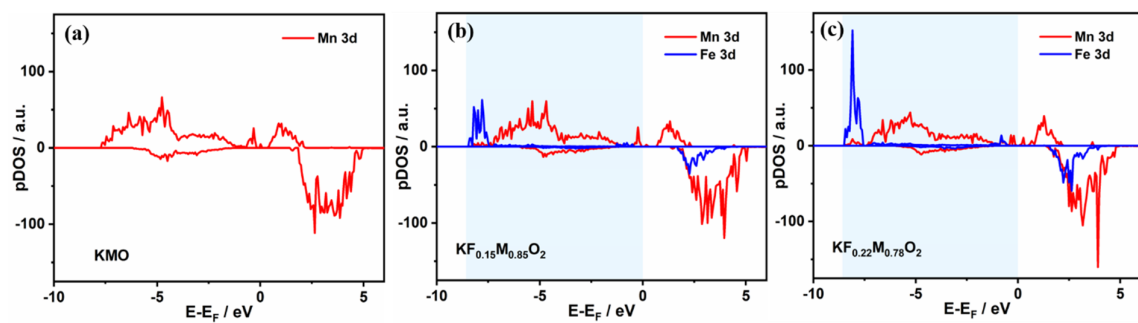


Figure S6. PDOS plots of the Mn 3d and Fe 3d orbitals of (a) KMO, (b) $\text{KF}_{0.15}\text{M}_{0.85}\text{O}_2$ and (c) $\text{KF}_{0.22}\text{M}_{0.78}\text{O}_2$.

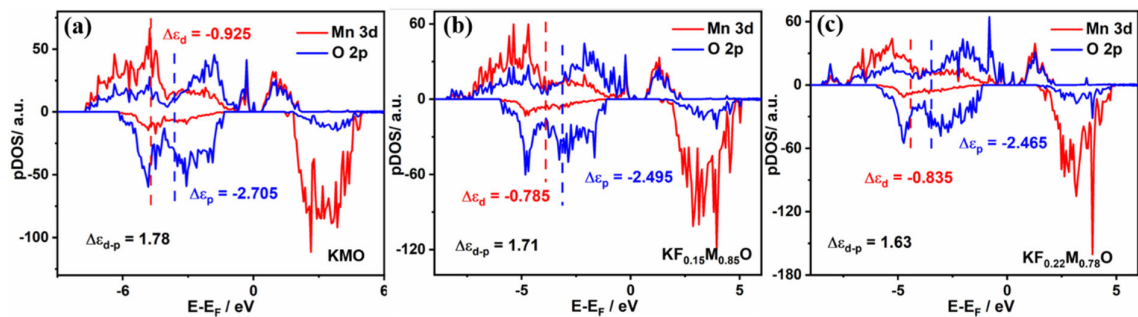


Figure S7. PDOS plots of the Mn 3d and O 2p orbitals of (a) KMO, (b) $\text{KFe}_{0.15}\text{Mn}_{0.85}\text{O}$ and (c) $\text{KFe}_{0.22}\text{Mn}_{0.78}\text{O}$.

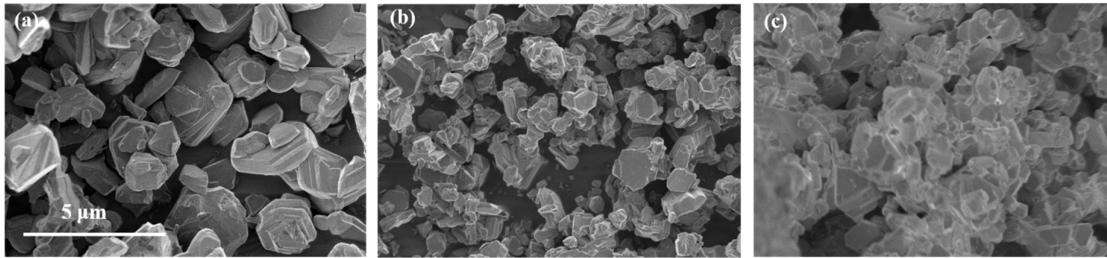


Figure S8. SEM images of (a) KMO, (b) $\text{KFe}_{0.15}\text{Mo}_{0.85}\text{O}_2$, (c) $\text{KFe}_{0.22}\text{Mo}_{0.78}\text{O}_2$ powder.

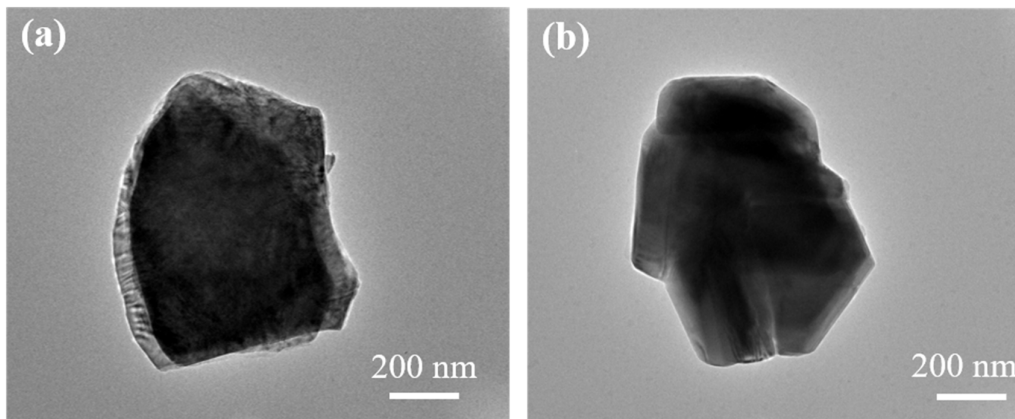


Figure S9. TEM images of (a) KMO and (b) $\text{KF}_{0.15}\text{M}_{0.85}\text{O}$ powder.

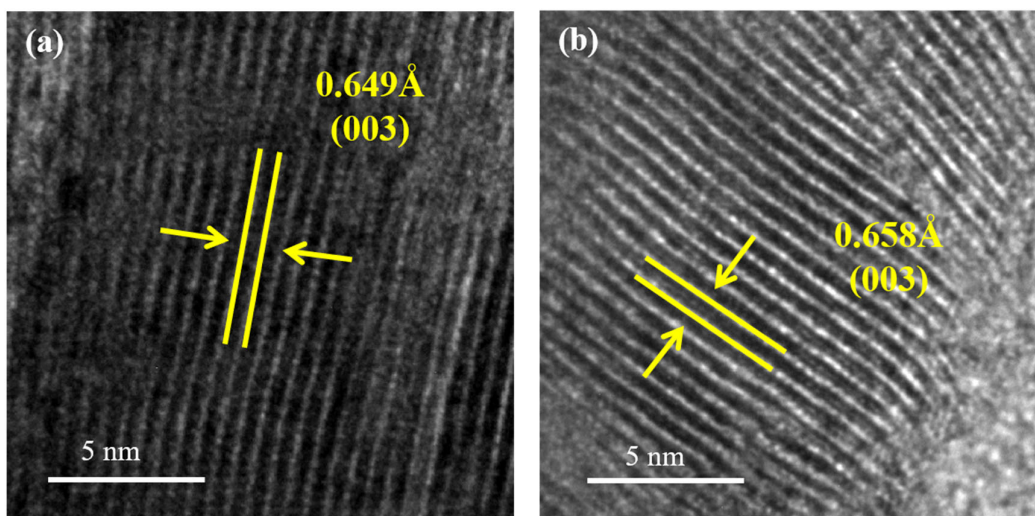


Figure S10. HR-TEM images of (a) KMO and (b) KF_{0.15}M_{0.85}O powder.

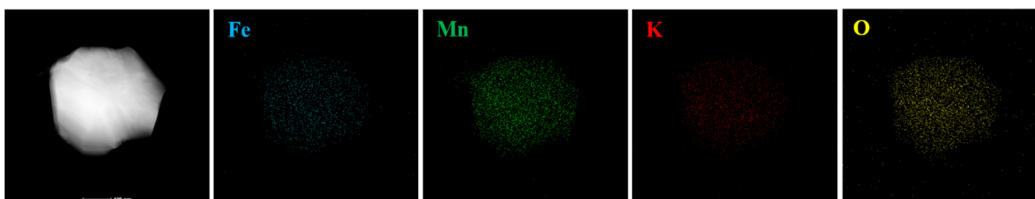


Figure S11. EDS mapping of $\text{KF}_{0.15}\text{Mn}_{0.85}\text{O}$ powder.

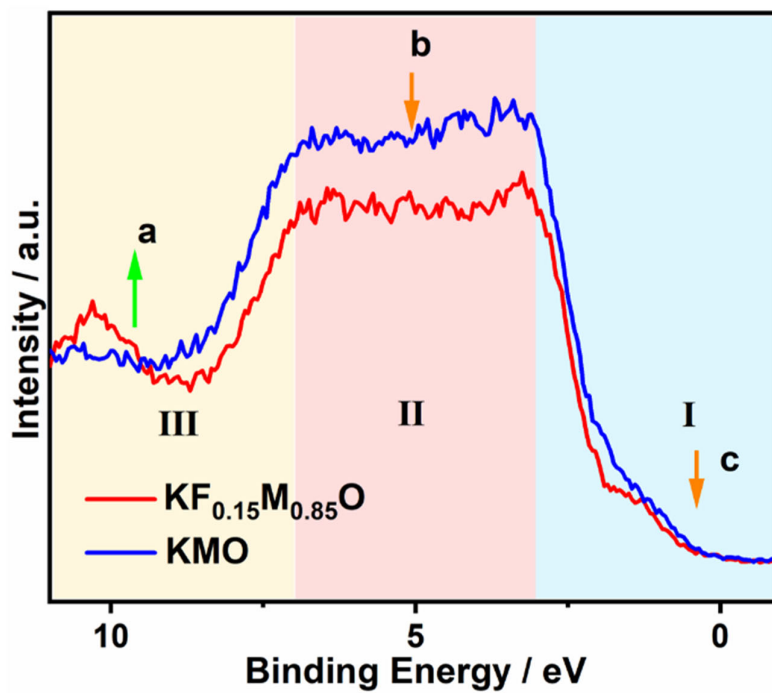


Figure S12. XPS valence band spectra of KMO and $\text{KF}_{0.15}\text{M}_{0.85}\text{O}$.

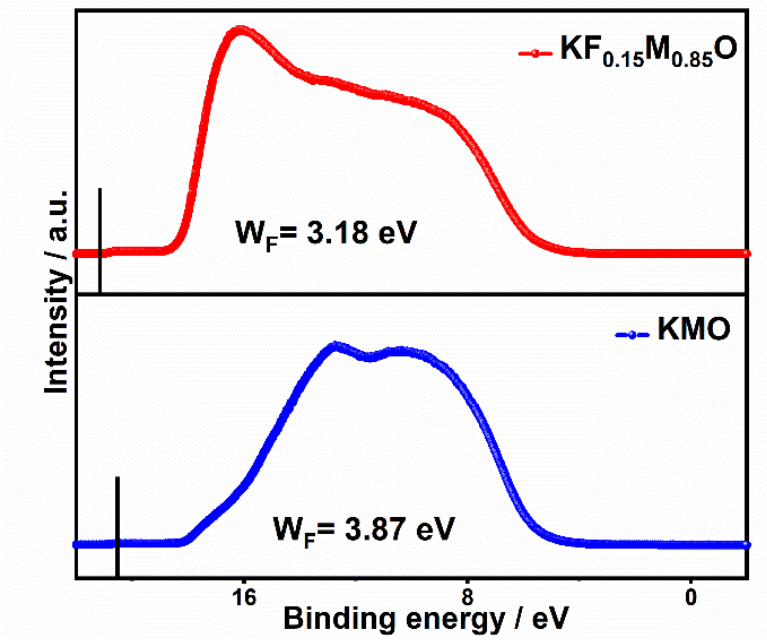


Figure S13. UPS of KMO and $\text{KF}_{0.15}\text{M}_{0.85}\text{O}$.

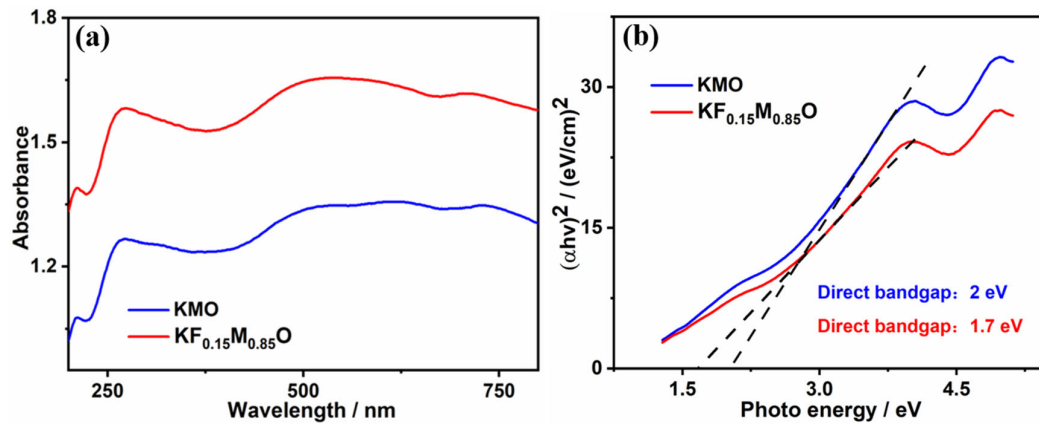


Figure S14. (a) UV-vis diffuse reflectance spectra and (b) bandgap energy of KMO and $\text{KF}_{0.15}\text{M}_{0.85}\text{O}$.

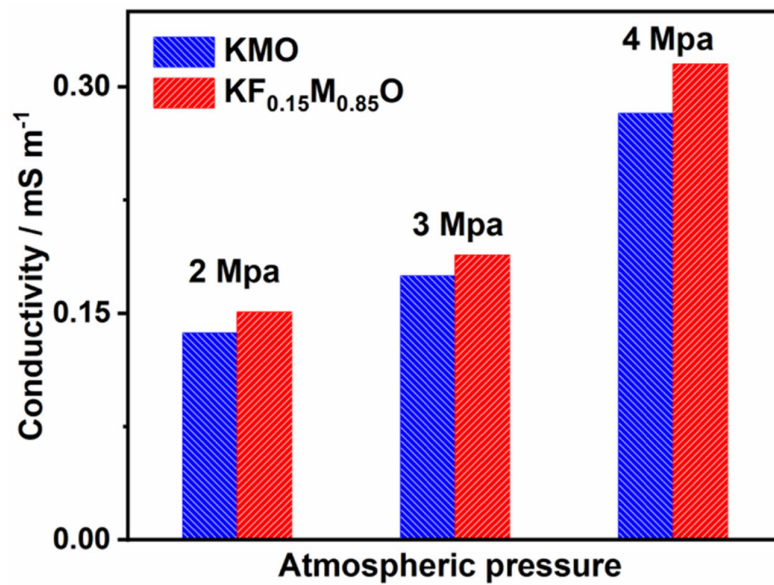


Figure S15. Measurement of the electrical conductivity of KMO and $\text{KF}_{0.15}\text{M}_{0.85}\text{O}$ using the four-probe method.

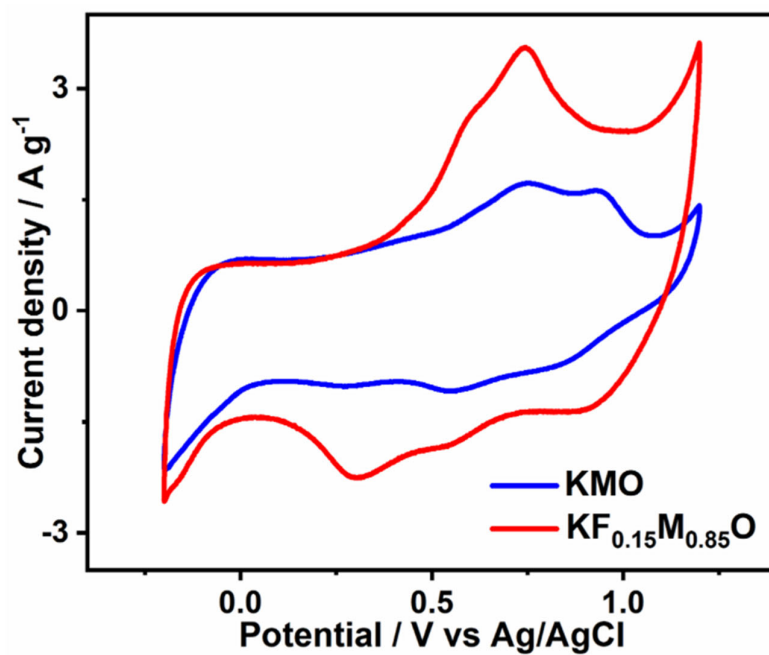


Figure S16. CV curves of KMO and $\text{KF}_{0.15}\text{M}_{0.85}\text{O}$ at 5 mV s^{-1} .

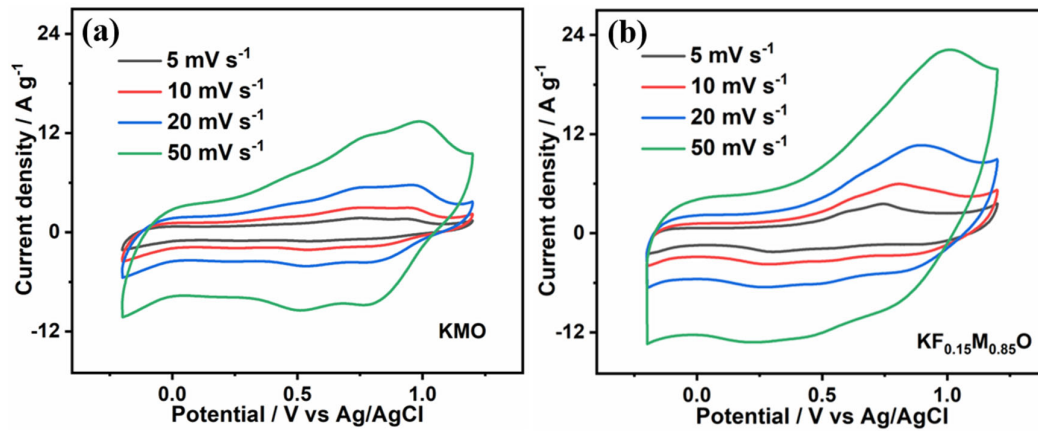


Figure S17. CV curves of (a) KMO and (b) KF_{0.15}M_{0.85}O electrode at different scan rates from 5 to 50 mV s⁻¹.

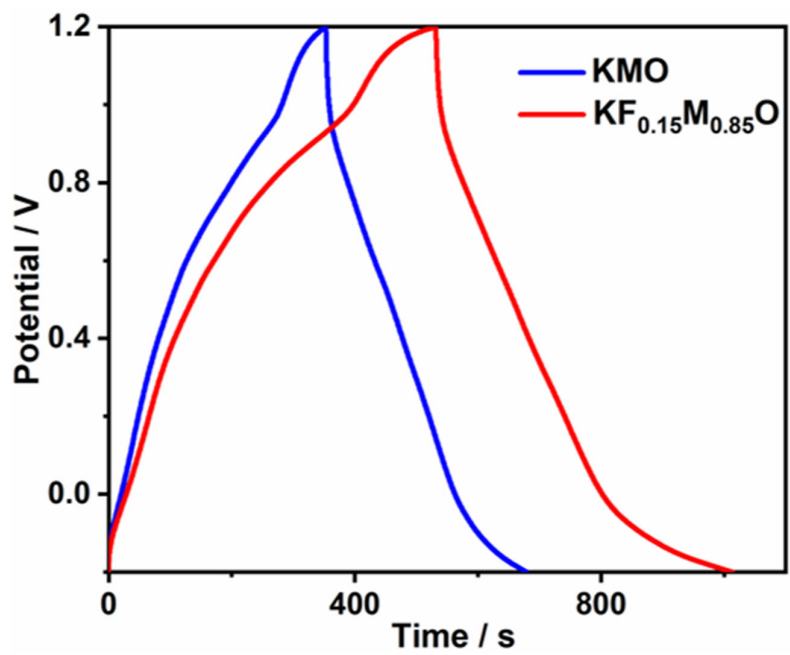


Figure S18. GCD curves of KMO and $\text{KF}_{0.15}\text{M}_{0.85}\text{O}$ electrode at 1 A g^{-1} .

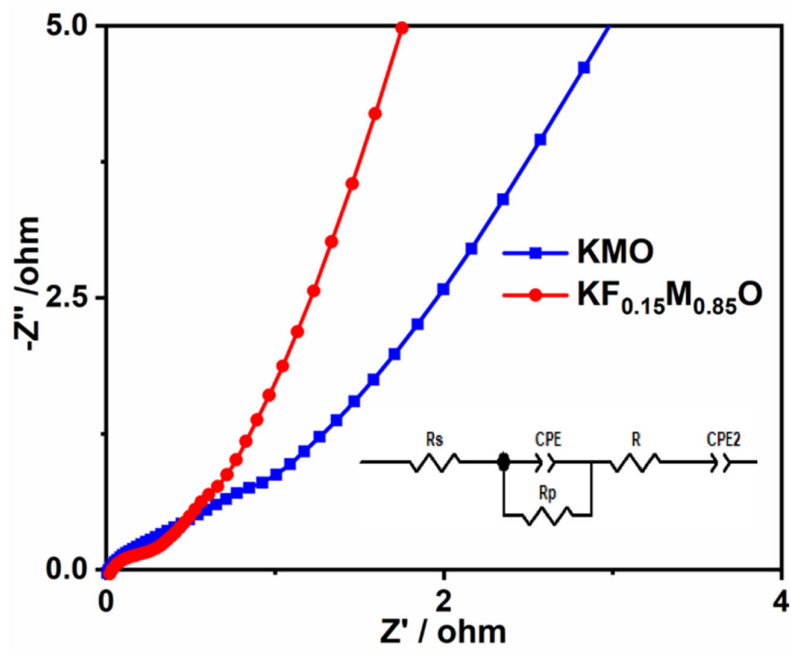


Figure S19. Nyquist plots of KMO and $\text{KF}_{0.15}\text{M}_{0.85}\text{O}$ in the pristine state.

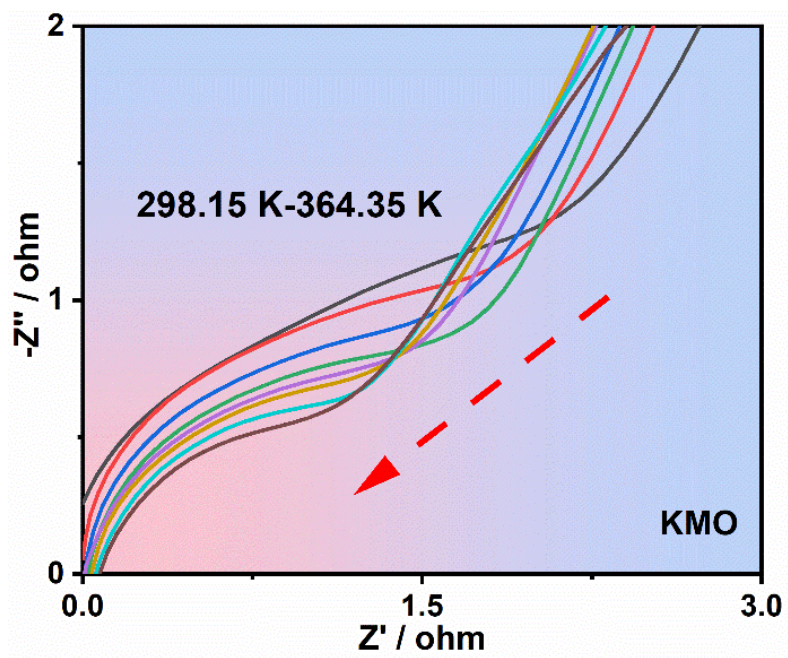


Figure S20. EIS study of KMO at varied temperatures.

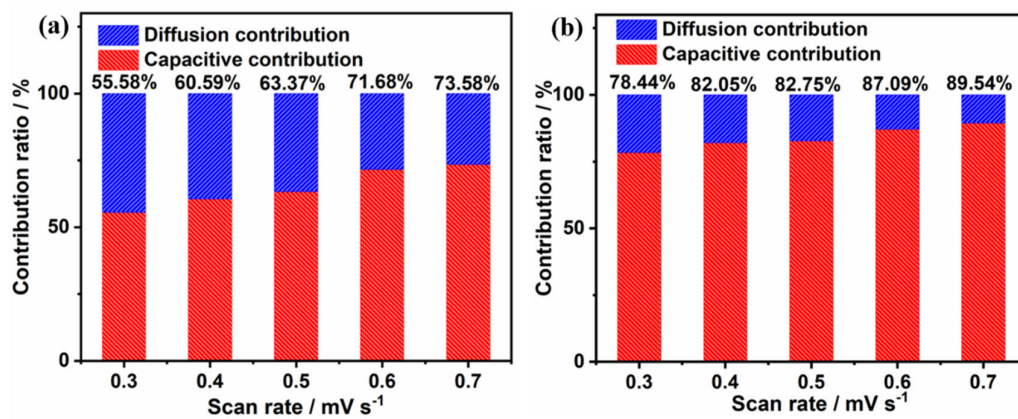


Figure S21. Capacity contribution from diffusion-controlled and surface-controlled processes at different scan rates for (a) KMO and (b) KFe_{0.15}Mo_{0.85}O.

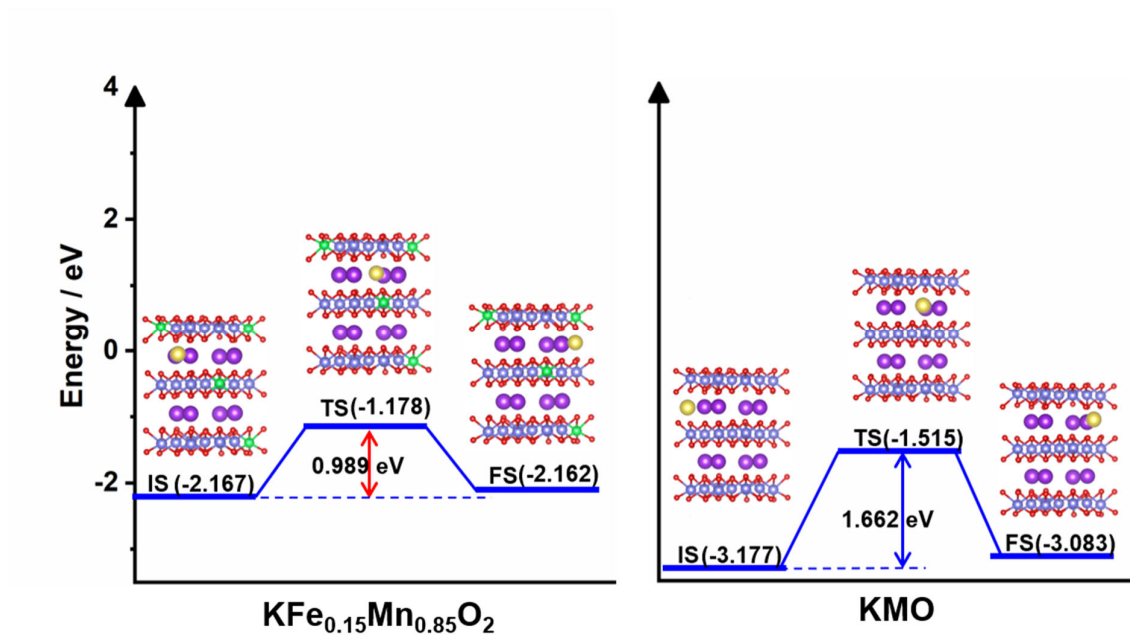


Figure S22. Energy curves and structures for Na⁺ diffusion in KFe_{0.15}Mn_{0.85}O and KMO models. The barriers in the energy curves are highlighted by a blue font. The purple, green, red, lavender and yellow colors represent the K, Fe, O, Mn and Na atoms, respectively.

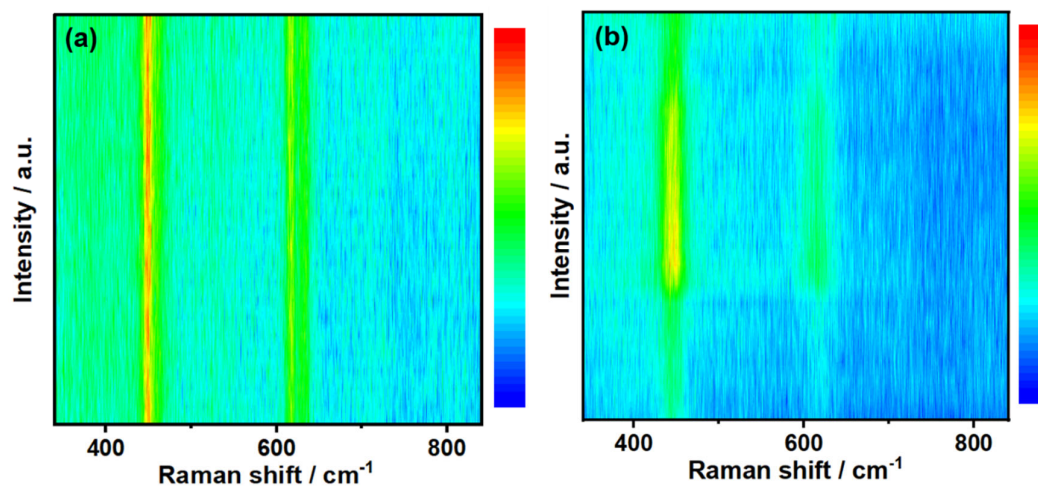


Figure S23. In situ Raman spectra of (a) KMO and (b) KFMO electrode during the first charge/discharge cycle.

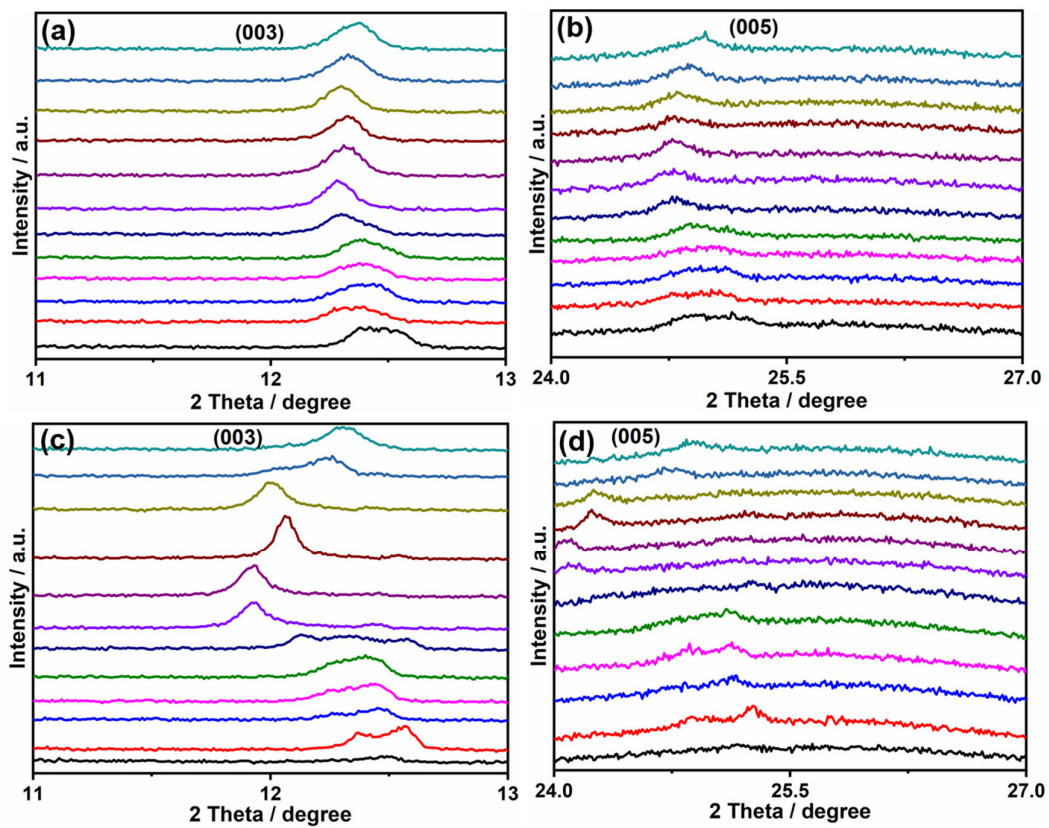


Figure S24. In-situ XRD patterns showing the peak shifts of the (003), and (005) planes for (a-b) KFMO and (c-d) KMO.

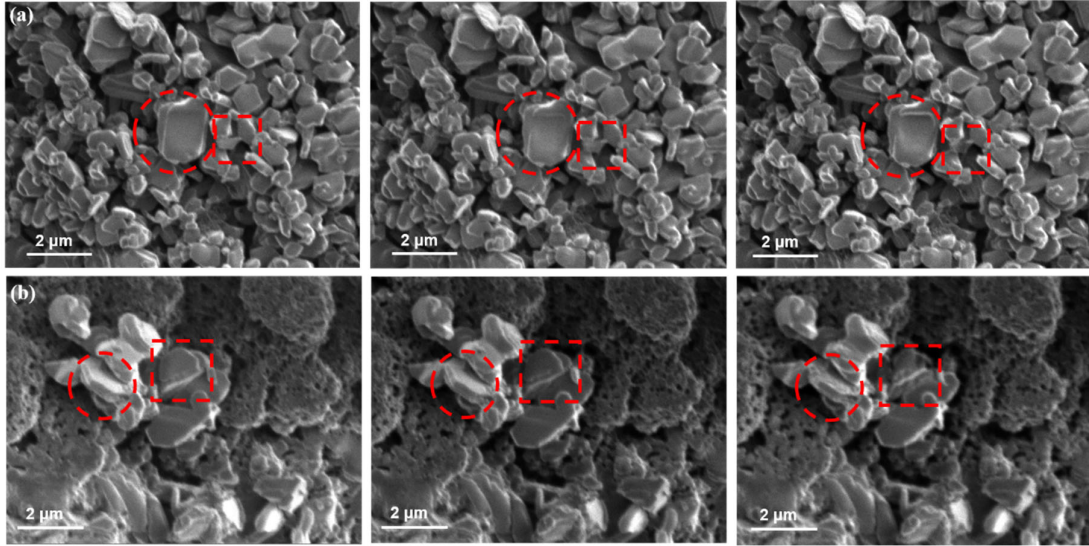


Figure S25. The cross-sectional SEM image of (a) $\text{KF}_{0.15}\text{M}_{0.85}\text{O}$ and (b) KMO after 200 cycles. The cross-sectional sample was prepared via the technology of focused ion beam (FIB).

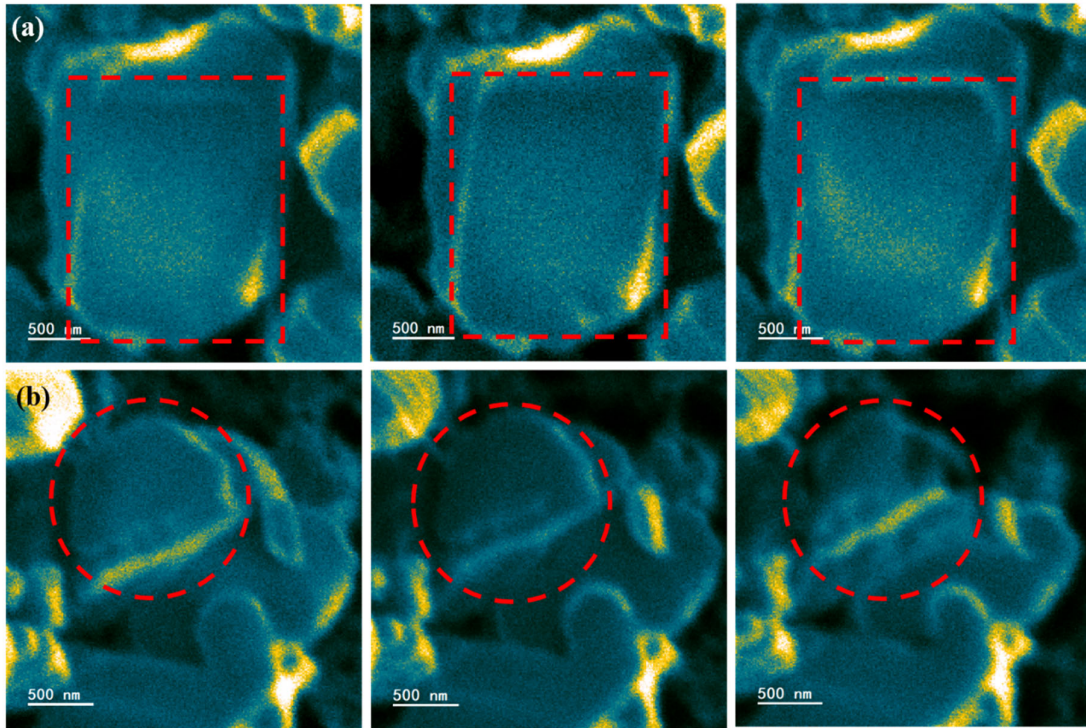


Figure S26. Local magnified SEM cross-sectional image of (a) $\text{KFe}_{0.15}\text{Mn}_{0.85}\text{O}$ and (b) KMO after 200 cycles. The cross-sectional sample was prepared via the technology of focused ion beam (FIB).

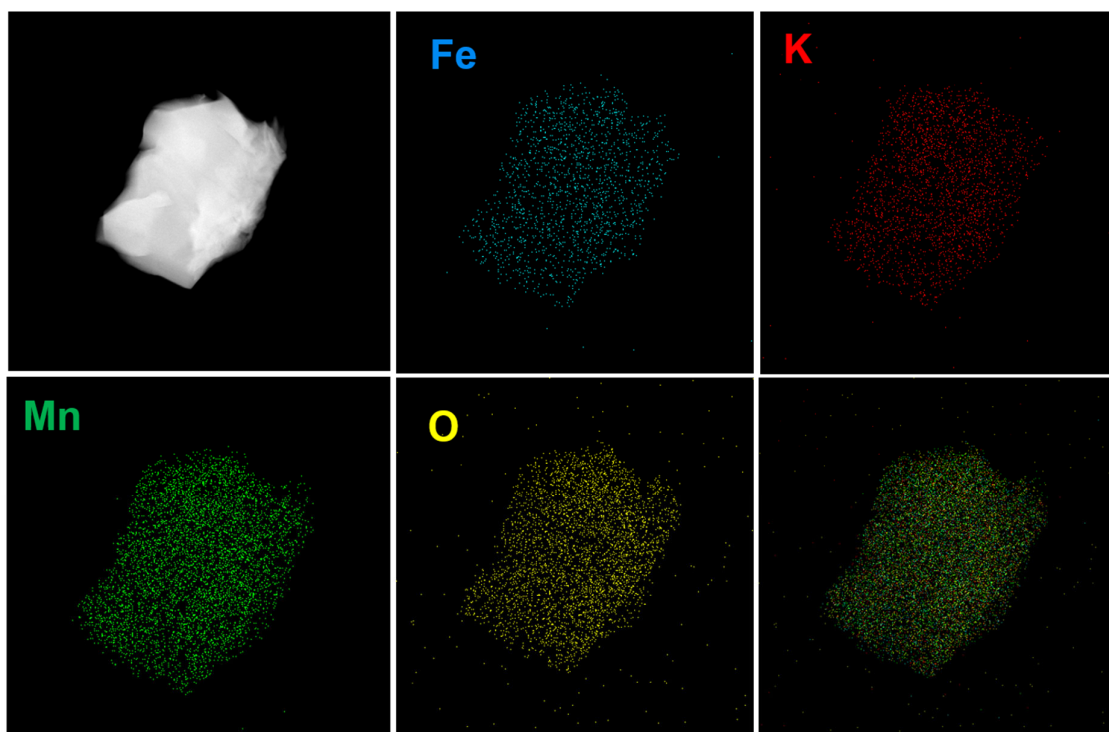


Figure S27. EDS elemental mapping of the KFMO electrode after 200 electrochemical cycles.

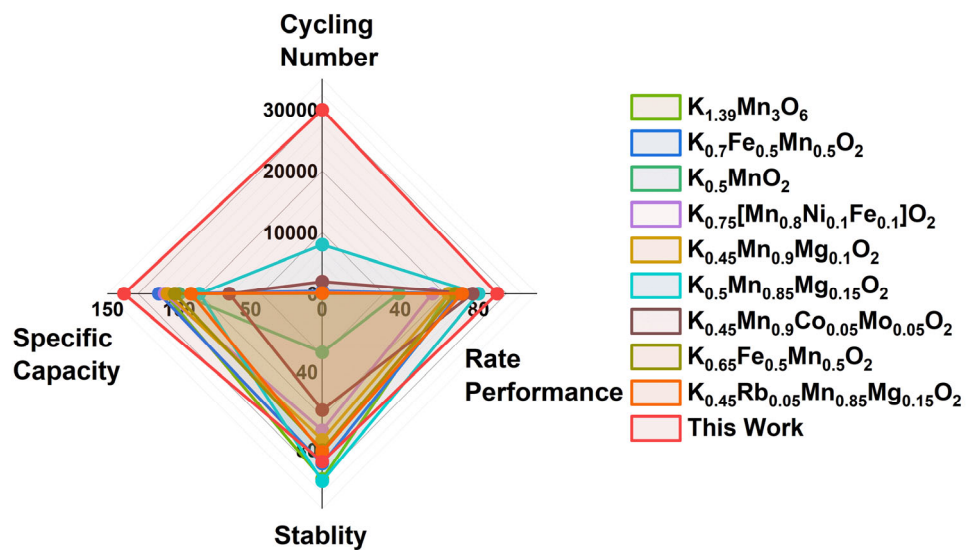


Figure S28. Comparative analysis: $\text{KF}_{0.15}\text{Mn}_{0.85}\text{O}$ cathode versus previous studies⁷⁻¹⁵.

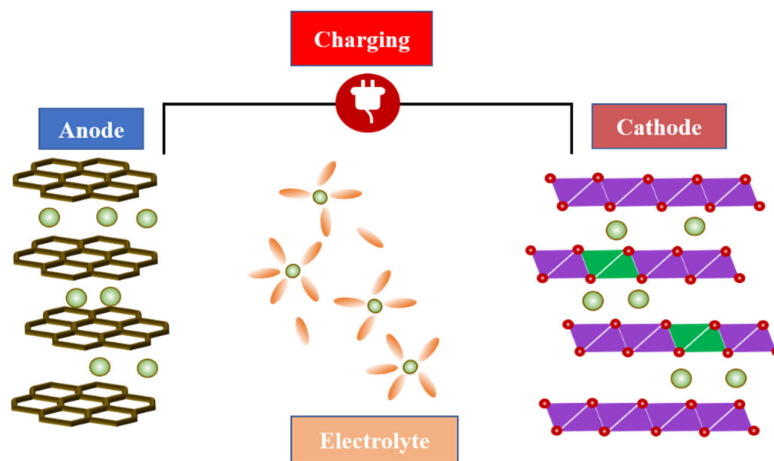


Figure S29. Schematic illustration of ASC based on $\text{KF}_{0.15}\text{M}_{0.85}\text{O}$ cathode and AC anode.

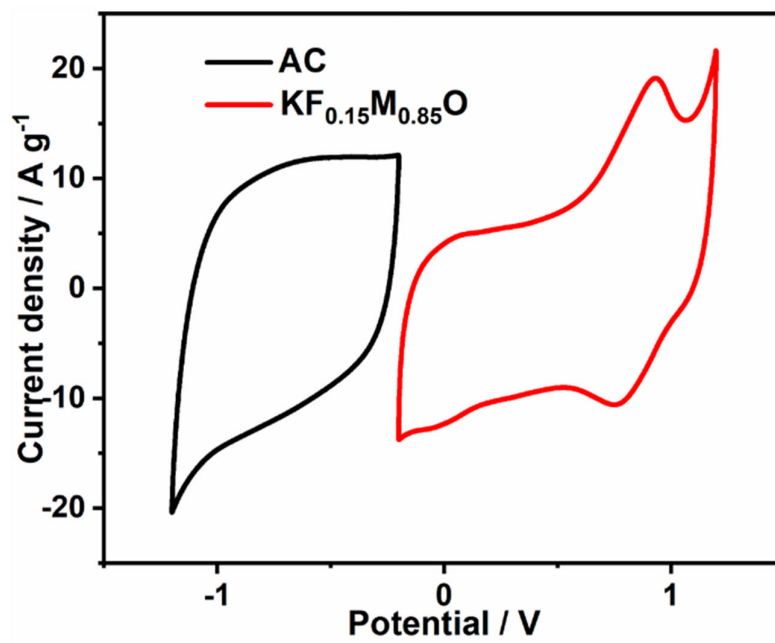


Figure S30. CV profiles of KF_{0.15}M_{0.85}O and AC in 1.0 M Na₂SO₄.

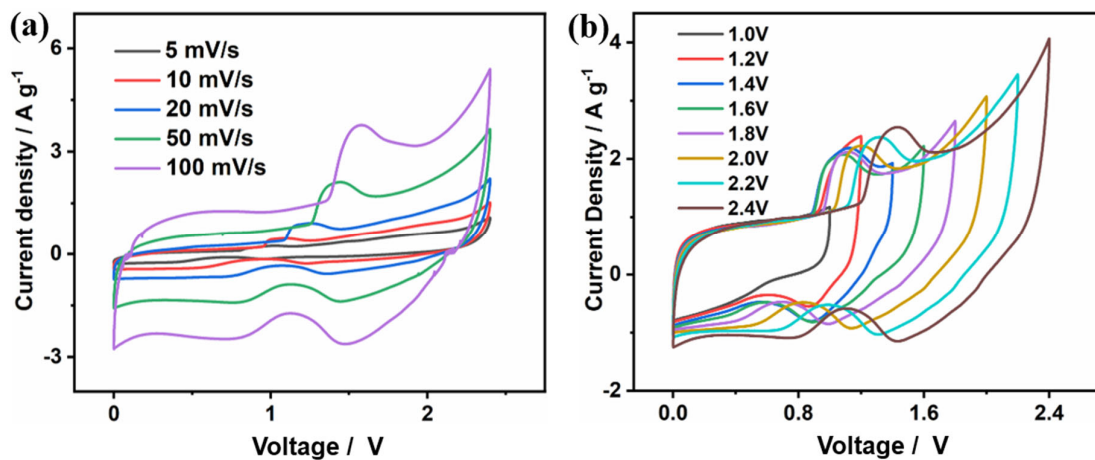


Figure S31. (a) CV profiles at varied potential ranges at 100 mV s^{-1} . (b) CV curves of $\text{KF}_{0.15}\text{M}_{0.85}\text{O} // \text{AC ASC}$ at various scan rates.

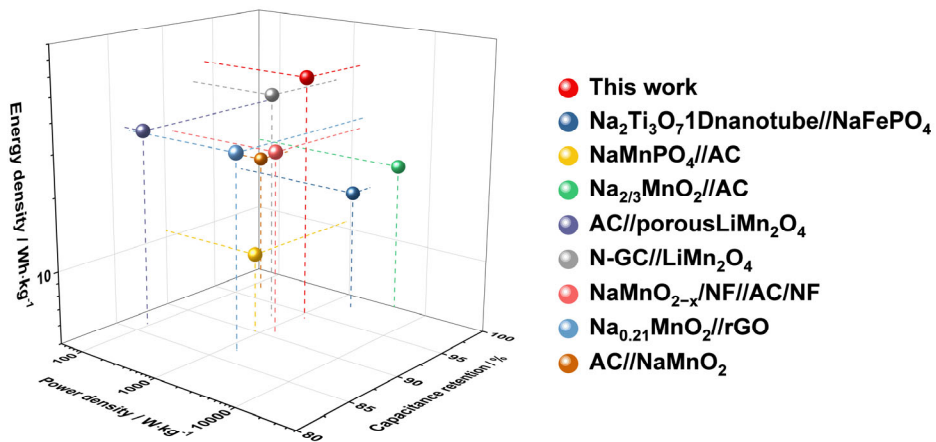


Figure S32. Comparative analysis of stability, power density, and energy density against previously reported results.¹⁶⁻²⁰

Table S1. Element contents of the samples obtained from element analysis Wt.%.

Sample	K element content Wt.%	O element content Wt.%	Mn element content Wt.%	Fe element content Wt.%
KMO	11.39	42.04	46.57	0
KF _{0.09} M _{0.91} O	11.49	58.31	27.28	2.92
KF _{0.15} M _{0.85} O	11.16	43.35	38.47	7.02
KF _{0.22} M _{0.78} O	11.41	44.83	33.89	9.87

Table S2. The *d*-electrons states proportion in $K_xFe_yMn_{1-y}O_z$ obtained from DOS.

Mn		t_{2g}			e_g	
		d_{xy}	d_{yz}	d_{xz}	d_z^2	$d_{x^2-y^2}$
DOS results	KMO	20.51	19.75	19.72	19.82	20.20
	$KF_{0.09}M_{0.91}O$	20.07	20.04	20.21	19.78	19.90
	$KF_{0.15}M_{0.85}O$	20.15	20.11	20.15	19.59	20.01
	$KF_{0.22}M_{0.78}O$	20.26	20.20	19.96	19.39	20.18
Fe		t_{2g}			e_g	
		d_{xy}	d_{yz}	d_{xz}	d_z^2	$d_{x^2-y^2}$
DOS results	$KF_{0.09}M_{0.91}O$	19.18	20.14	19.62	21.75	19.30
	$KF_{0.15}M_{0.85}O$	19.74	21.38	18.66	19.30	20.93
	$KF_{0.22}M_{0.78}O$	21.46	19.45	21.70	17.02	20.38

Table S3. -COHP analysis of KMO, $\text{KF}_{0.15}\text{Mn}_{0.85}\text{O}$ and $\text{KF}_{0.22}\text{Mn}_{0.78}\text{O}$.

Atoms in KMO	-COHP (eF)	Atoms in $\text{KF}_{0.15}\text{Mn}_{0.85}\text{O}$	-COHP (eF)	Atoms in $\text{KF}_{0.22}\text{Mn}_{0.78}\text{O}$	-COHP (eF)
Mn67-O4	0.392	Mn72-O4	1.102	Mn71-O4	1.305
Mn67-O6	0.932	Mn72-O6	1.247	Mn71-O6	1.589
Mn67-O8	1.079	Mn72-O8	1.122	Mn71-O8	1.436
Mn67-O14	1.162	Mn72-O14	1.126	Mn71-O14	1.504
Mn67-O16	1.048	Mn72-O16	1.124	Mn71-O16	1.380
Mn67-O17	0.407	Mn72-O17	1.174	Mn71-O17	1.447
average	0.837	average	1.149	average	1.444

Table S4. Fitting results of KMO and $\text{KF}_{0.15}\text{M}_{0.85}\text{O}$ samples obtained from the EIS curves.

	R_e (combined resistance)	C_{dl} (double- layer capacitance)	R_{ct} (charge transfer resistance)	Z_w (Warburg resistance)
KMO	5.20	0.81	4.60	2.61
$\text{KF}_{0.15}\text{M}_{0.85}\text{O}$	5.87	0.66	0.73	1.28

Supplementary References:

1. R. Kang, D. Zhang, H. Wang, B. Zhang, X. Zhang, G. Chen, Y. Du and J. Zhang, *Energy Environ. Sci.*, 2024, **17**, 7135-7146.
2. Y. Hu, Y. Wu and J. Wang, *Adv. Mater.*, 2018, **30**, e1802569.
3. Y. Shao, M. F. El-Kady, J. Sun, Y. Li, Q. Zhang, M. Zhu, H. Wang, B. Dunn and R. B. Kaner, *Chem. Rev.*, 2018, **118**, 9233-9280.
4. J. Sun, C. Wu, X. Sun, H. Hu, C. Zhi, L. Hou and C. Yuan, *J. Mater. Chem. A*, 2017, **5**, 9443-9464.
5. P. E. Blöchl, *Phys. Rev. B*, 1994, **50**, 17953-17979.
6. G. Kresse and J. Furthmüller, *Phys. Rev. B: Condens. Matter*, 1996, **54**, 11169-11186.
7. S. Zhao, K. Yan, P. Munroe, B. Sun and G. Wang, *Adv. Energy Mater.*, 2019, **9**, 1803757.
8. X. Wang, X. Xu, C. Niu, J. Meng, M. Huang, X. Liu, Z. Liu and L. Mai, *Nano Lett.*, 2017, **17**, 544-550.
9. H. Kim, D. H. Seo, J. C. Kim, S. H. Bo, L. Liu, T. Shi and G. Ceder, *Adv. Mater.*, 2017, **29**, 1702480.
10. J.-Y. Hwang, J. Kim, T.-Y. Yu, H.-G. Jung, J. Kim, K.-H. Kim and Y.-K. Sun, *J. Mater. Chem. A*, 2019, **7**, 21362-21370.
11. C. I. Liu, S. h. Luo, H. b. Huang, Y. c. Zhai and Z. w. Wang, *ChemElectroChem.*, 2019, **6**, 2308-2315.
12. C. Zhou, L. Li, Z. Dong, F. Lv, H. Guo, K. Wang, M. Li, Z. Qian, N. Ye, Z. Lin, M. Luo and S. Guo, *Nat. Commun.*, 2024, **15**, 9774.
13. W. Han, X. W. Gao, Y. Song, X. Wang, G. Gao, H. Chen, Q. Gu and W. B. Luo, *Small*, 2024, **20**, e2400252.
14. T. Deng, X. Fan, J. Chen, L. Chen, C. Luo, X. Zhou, J. Yang, S. Zheng and C. Wang, *Adv. Funct. Mater.*, 2018, **28**, 1800219.
15. Z. Caixiang, J. Hao, J. Zhou, X. Yu and B. Lu, *Adv. Energy Mater.*, 2022, **13**, 2203126.
16. S. Xu, T. Wan, K.-b. Zhou, G.-m. Zhu, Z.-q. He, H.-b. Huang, T. Zhou, W.-q. Mao, J.-j. Wu, S.-k. Gong and Y.-x. Qiao, *Mater. Res. Express*, 2020, **7**, 035508.
17. H. Xiao, Y. Wang, K. Xie, S. Cheng and X. Cheng, *J. Alloy. Compd.*, 2018, **738**, 25-31.
18. A. A. Nechikott and P. K. Nayak, *RSC Adv.*, 2023, **13**, 14139-14149.
19. P. De, D. Mandal, S. Biswas, A. Kumar, S. Priya, B. K. Dubey, A. K. Srivastava and A. Chandra, *Energ. Fuel.*, 2023, **37**, 5595-5606.
20. S. Biswas, D. Mandal, T. Singh and A. Chandra, *RSC Adv.*, 2021, **11**, 30031-30039.